Journal of Alloys and Compounds, 194 (1993) 311–317
JALCOM 7218

On the influence of gaseous impurities in the amorphization reaction of some titanium-based alloys

J. Hunt[a], I. Soletta[b], L. Battezzati[c], N. Cowlam[a] and G. Cocco[b]

[a]*Department of Physics, University of Sheffield, Sheffield, S3 7RH (UK)*
[b]*Dipartimento di Chimica, Università di Sassari, Via Vienna 2, 07100 Sassari (Italy)*
[c]*Dipartimento di Chimica Inorganica, Chimica Fisica e Chimica dei Materiali, Università di Torino, Via P. Giuria 9, 10125 Torino (Italy)*

(Received December 9, 1991; in final form July 22, 1992)

Abstract

Some titanium-based alloys were examined by X-ray and neutron diffraction and differential scanning calorimetry (DSC) as part of a continuing research programme on amorphous alloys produced by mechanical alloying (MA). Large differences were found between the X-ray and neutron diffraction patterns on the same materials, which can be understood in terms of the relative visibilities of the alloy constituents for the two radiations. The neutron diffraction patterns provide unequivocal evidence that the alloys contain both amorphous and crystalline phases. A characteristic series of broad Bragg peaks was observed in the neutron diffraction patterns of amorphous Cu–Ti, Pd–Ti and Al–Ti alloys which was not evident when using X-rays. These peaks were identified with a mixed oxide–nitride Ti(O, N) impurity phase. DSC analysis of selected milling products revealed the transformation of the metastable phases. It also provided enthalpy data for a thermodynamic description of the milling process. These observations provide support to our previous findings on the significance of gaseous impurities of the parent metals in the MA process.

1. Introduction

The production of amorphous metal alloys by the technique of mechanical alloying (MA) is one of the so-called "solid-state reactions" which are currently the subject of worldwide interest [1]. In many cases it is possible to produce genuine amorphous alloys whose structures can stand scrutiny by the most sensitive techniques. In Fig. 1, for example, the structure factors $S(Q)$ of two amorphous Cu–Ti alloys produced by 16 h of MA treatment are given, with the structure factors of copper-rich Cu–Ti metallic glasses [2] shown in the inset for comparison. It can be seen that there is little doubt about the amorphous nature of either kind of sample. However, there are other cases in which the amorphization reaction may be incomplete for various reasons.

In recent investigations of a-Cu–Ti ("a" indicates amorphous) alloys produced by MA we have found evidence to indicate that hydrogen contamination can influence the course of the reaction. Specifically, a first series of Cu_xTi_{100-x} alloys with $75>x>30$ was made with titanium containing a small amount of hydrogen contamination; these alloys were found to be amorphous over the whole composition range studied [3]. A second series of samples was made with titanium which was free of hydrogen. After a similar period (16 h) of MA treatment, the reaction proceeded to completion only in the copper-rich samples, while in the titanium-rich samples the reaction was incomplete. These latter specimens consisted of a mixture of the intermetallic compounds γ-CuTi and $CuTi_2$ [4]. It appears therefore that hydrogen can play an active part in the reaction and that in its absence the reaction may be inhibited. Indeed, a further demonstration of these effects has been given by the mechanical milling (MM) of the crystalline phase γ-CuTi in both argon and hydrogen atmospheres [5]. Only in the latter case can large fractions of amorphous phase be produced. These are potentially very interesting observations because they make contact with the hydrogen amorphization reaction, first found in Zr_3Rh–H [6] and recently extended to many rare earth–transition metal compounds [7].

With hindsight, it might have been expected that the use of finely divided powders in the MA process (particularly of active materials such as titanium and zirconium) would lead to problems with gaseous contamination. However, it is clearly inadvisable to bypass these problems by using starting materials of higher purity since, as we have shown, the impurities clearly

0925-8388/93/$6.00

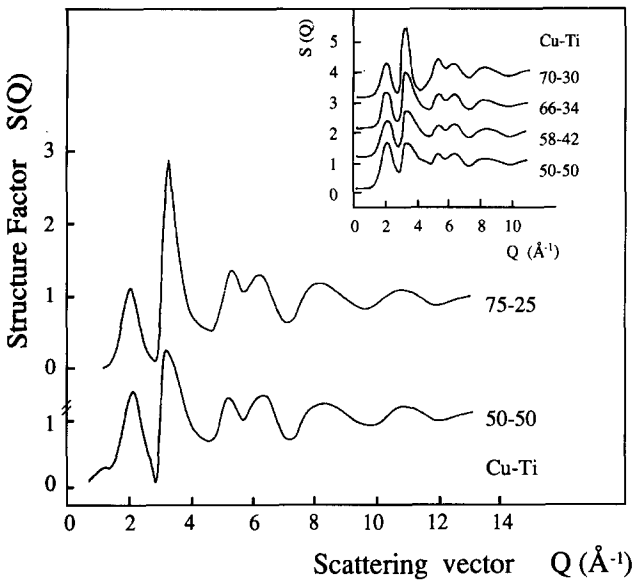

Fig. 1. Structure factors $S(Q)$ for $Cu_{75}Ti_{25}$ and $Cu_{50}Ti_{50}$ amorphous alloys obtained using the D20 neutron diffractometer at the Institut Laue-Langevin (ILL), Grenoble. The equivalent curves for CuTi metallic glasses are shown in the inset (after Sakata *et al.* [2]). Both sets of curves give clear indications of the amorphous nature of the specimens.

influence the amorphization process itself. In addition, they will certainly be present in any future technological or industrial applications of MA in which materials of laboratory grade are unlikely to be used.

Fortunately one long established advantage of neutron scattering over X-rays is in the detection of light atoms, although this is usually taken to mean via the coherent neutron scattering rather than the incoherent scattering detected in our experiment on Cu–Ti samples. Thus neutron diffraction is able to provide direct information on the gaseous impurities in mechanically alloyed samples. However, this apparent advantage is sometimes complicated by the fact that X-ray and neutron diffraction patterns of the same mechanically alloyed materials can be very different. These differences, which are much larger than expected, originate from the variations in the scattering amplitudes of the alloy constituents for X-rays and neutrons, which are complicated by the "negative" or resonant neutron scattering from the titanium nuclei (see refs. 3 and 4). The work described below mainly concerns samples from a series specially prepared for a third allocation of neutron beam time on the D20 diffractometer at the Institut Laue–Langevin (ILL), Grenoble. These experiments were aimed at extending the range of mechanically alloyed samples measured and were augmented by differential scanning calorimetry (DSC) measurements intended to provide data for a thermodynamic description of the process.

2. Sample preparation and experimental procedure

In the sample preparation appropriate amounts of powders were milled in a hardened steel vial using a Spex mixer-mill (model 8000) with three hardened steel balls (diameter, $\frac{1}{2}$ in). Milling was carried out at room temperature under an argon atmosphere to prevent oxidation and heat was removed by a fan working in front of the milling tool. The powders were of the following specification: titanium, Ventron 99% 325 mesh (found to be contaminated by approximately 15 at.% hydrogen) and Alfa Products 99.99% 200 mesh (hydrogen free); copper, Alfa Products 99.9% 325 mesh; aluminium, Johnson Matthey 99.8% 325 mesh; palladium, Metalli Preziosi 99.8% sponge. The weight of the starting powder was 3 g for Cu–Ti and Al–Ti alloys and 2 g for Pd–Ti. The milling times are given in the figures (see Section 3). The samples were examined immediately after the MA treatment in order to confirm their structure. X-Ray intensities were collected in a high-resolution mode using a Siemens D500 diffractometer connected with a highly stabilized generator. The angular range from 20° to 120° in 2θ was repeatedly scanned in steps of 0.05° in 2θ in the preset-time mode until a satisfactory signal-to-noise ratio was reached. The neutron scans were made using the D20 diffractometer at the ILL. A copper monochromator was used giving an incident neutron wavelength λ of 0.94 Å. The samples were examined in thin-walled vanadium tubes (external diameter, 7 mm) filled to a depth of approximately 15 mm and placed at the centre of an evacuated cloche. A typical scan was made by moving the multidetector (whose elements are spaced 0.01°) in steps of 3° from 4° to 142° with a count time of the order of 200 s per step. This gave a usable angular range in 2θ of 4°–155° and a scan time of approximately 3 h. A preliminary scan was made using a silicon standard in order to calibrate the wavelength and calculate the zero-offset in 2θ. Background and calibration scans were made using the empty vanadium tube and a 7 mm vanadium rod respectively. The multidetector data were corrected for zero-offset and individual detector efficiency and regrouped as intensity *vs.* scattering angle 2θ for plotting as a conventional diffraction pattern.

The thermal behaviour of the milled powders was investigated by DSC using a Perkin–Elmer DSC7 instrument. Aluminium crucibles were employed for scans up to 600 °C and gold crucibles up to 725 °C. Samples crimped in sealable aluminium crucibles were used when needed, in order to contain the hydrogen evolved on heating. All analyses were carried out with the crucibles in a flow of argon gas.

3. Experimental observations

Figures 2 and 3, which give the neutron and X-ray diffraction patterns for two pairs of Cu–Ti and Al–Ti specimens, illustrate the apparently conflicting results which the two radiations may provide. In the case of $Cu_{40}Ti_{60}$ the X-ray pattern of the 25 h sample shows a broad and fairly symmetrical halo indicative of a well transformed sample, although there is also evidence of a small broadened Bragg peak which is from crystalline TiH_2. The halo for the 42 h sample is less symmetrical, but there is no direct evidence of Bragg peaks from crystalline phases. In contrast, the neutron diffraction pattern of the 25 h sample exhibits the characteristic large decrease in intensity as a function of the scattering angle. This behaviour is typical of scattering from materials containing hydrogen. Hydrogen has the largest incoherent neutron scattering cross-section of all the elements, and so its presence in the sample, even in small quantities, is easily noticed. The scattered intensity is not only high, but has a characteristic angular dependence due to the departure from the so-called "static approximation" [8] which is, of course, largest for light atoms such as hydrogen. In addition to the sloping background, this pattern has two small, sharp, Bragg peaks arising from crystalline TiH_2. However, the oscillating background shows that a reasonable volume fraction of the starting materials has transformed to an amorphous state. The neutron diffraction pattern of the 42 h sample lacks the sloping background and consists of a regular series of broad Bragg peaks, with evidence of a coexisting amorphous phase from the oscillations in the background scattering. The equivalent data for the two mechanically alloyed $Al_{25}Ti_{75}$ samples are shown in Fig. 3. The neutron diffraction patterns of both samples show sloping backgrounds due to inelastic neutron scattering from the hydrogen atoms. This effect is larger for the 33 h sample showing that it is significantly contaminated by hydrogen. Moreover, both patterns provide evidence of an amorphous phase in the characteristic slow oscillations superimposed on the monotonically decreasing background. In the pattern of the 14 h sample a third major contribution to the intensity distribution is also evident: Bragg peaks of the kind observed in the $Cu_{40}Ti_{60}$ 42 h sample are the predominant feature and these may also be traced into the pattern of the 33 h specimen. The corresponding X-ray results are depicted in the inset. The pattern of the 33 h sample shows only broad haloes characteristic of an amorphous structure, whereas that of the 14 h sample presents roughly outlined crystalline peaks; it is worth noting that these crystalline features can be assigned to an unalloyed amount of titanium and that this contribution is absent in the relevant neutron pattern. This point is discussed in detail later.

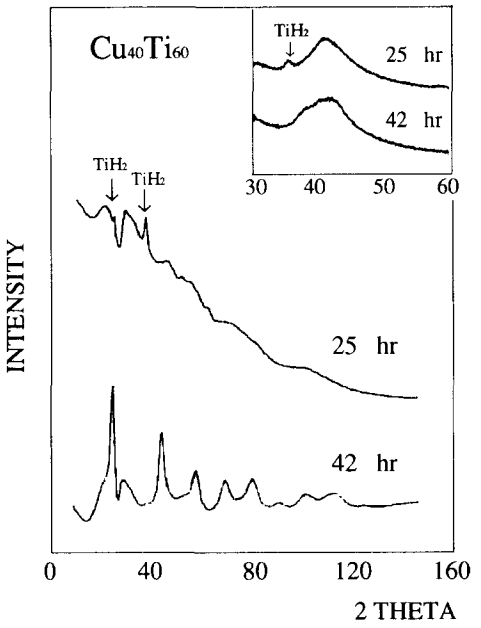

Fig. 2. Neutron diffraction patterns of two $Cu_{40}Ti_{60}$ samples after 25 h and 42 h of MA treatment. The Cu Kα X-ray diffraction patterns, through the first amorphous halo, are given in the inset for the same sample materials.

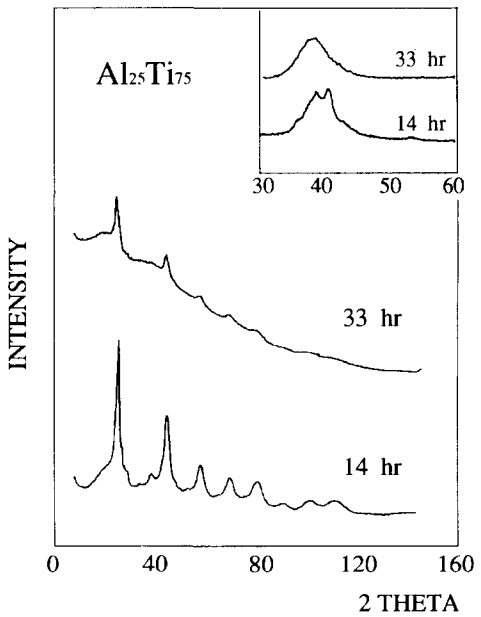

Fig. 3. Neutron diffraction patterns of two $Al_{25}Ti_{75}$ samples after 14 h and 33 h of MA treatment. The Cu Kα X-ray diffraction patterns, through the first amorphous halo, are given in the inset for the same sample materials.

These findings can be summarized as follows: for $Cu_{40}Ti_{60}$ both X-ray and neutron patterns provide some evidence of hydrogen contamination in the 25 h sample (the latter radiation most convincingly); the 42 h sample appears to be amorphous when using X-rays, but is clearly seen to be a mixture of crystalline and amorphous phases when using neutrons; the $Al_{25}Ti_{75}$ samples are

both contaminated with hydrogen and both contain crystalline phases; neither the hydrogen contamination nor the crystalline fraction in the 33 h sample was detected with X-rays.

Thermal analysis can provide complementary information on the gaseous impurities in these samples. The most extensive work has been carried out on the copper–titanium system. Two typical DSC traces for amorphized materials are shown in Fig. 4. That referring to $Cu_{50}Ti_{50}$ mechanically alloyed for 8 h (upper curve) displays a sharp exothermal peak due to the polymorphous crystallization of the alloy to the γ-CuTi compound [9]. The lower curve in Fig. 4 refers to $Cu_{40}Ti_{60}$ mechanically alloyed for 16 h which was prepared using a parent titanium powder containing 15 at.% of hydrogen. A huge endothermal signal is the main feature in the trace which is the manifestation of hydrogen evolution from the alloy. The sample cell of the instrument is separated from the reference cell, while both are kept under argon, and experiences a different atmosphere when hydrogen is released. Because of the high thermal conductivity of hydrogen, the thermal balance between the cells is strongly perturbed and the crystallization cannot be detected. It is probable that it starts before the onset of hydrogen desorption, as the DSC trace tends to bend downwards in the exothermal sense. For some of the hydrogen-contaminated amorphous alloys the crystallization peak becomes clearer in scans performed with samples enclosed in sealed crucibles so that the hydrogen evolved is confined in the volume of the crucible. In the majority of cases further heating of the sample causes the leakage of gas from the crucible with an immediate consequence on the thermal balance between the cells.

The enthalpy release on crystallization is definitely lower for the hydrogenated alloys (values around -3.5 kJ mol^{-1}) than for the hydrogen-free materials (values around -6 kJ mol^{-1}). This can be easily understood by considering that the transformation products of the hydrogenated samples include the appropriate mixture of intermetallics and the TiH_2 phase [10].

4. Identification of the oxide–nitride phase

The strong intensities and the regularity of spacing of the Bragg peaks in the neutron diffraction patterns of the $Cu_{40}Ti_{60}$ (25 h) and $Al_{25}Ti_{75}$ (14 h) samples mean that they can easily be identified when present in the diffraction patterns of the other titanium-based alloys examined. Figure 5 shows a series of five neutron diffraction patterns from D20, from the $Cu_{40}Ti_{60}$ sample mechanically alloyed for 42 h, two $Pd_{40}Ti_{60}$ samples mechanically alloyed for 9 and 26 h and two $Al_{25}Ti_{75}$ samples mechanically alloyed for 14 and 21 h. The similarities between the patterns are striking. However, close inspection shows that there are contributions due to scattering from an amorphous phase for at least three and perhaps all of the samples. The pattern for $Cu_{40}Ti_{60}$ shows that the first Bragg peak sits on a broad feature whose maximum corresponds in angle to $Q = 1.9$ Å^{-1}, the position of the pre-peak in $S(Q)$ [3], while

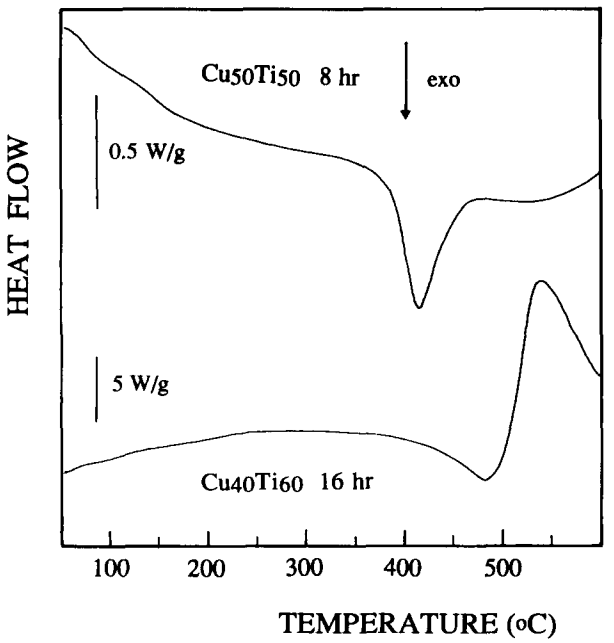

Fig. 4. DSC traces for a hydrogen-free $Cu_{50}Ti_{50}$ alloy mechanically alloyed for 8 h (upper curve) and a hydrogen-contaminated $Cu_{40}Ti_{60}$ alloy mechanically alloyed for 16 h (lower curve). Both alloys were prepared by MA and their structures appeared to be amorphous with both X-ray and neutron diffraction.

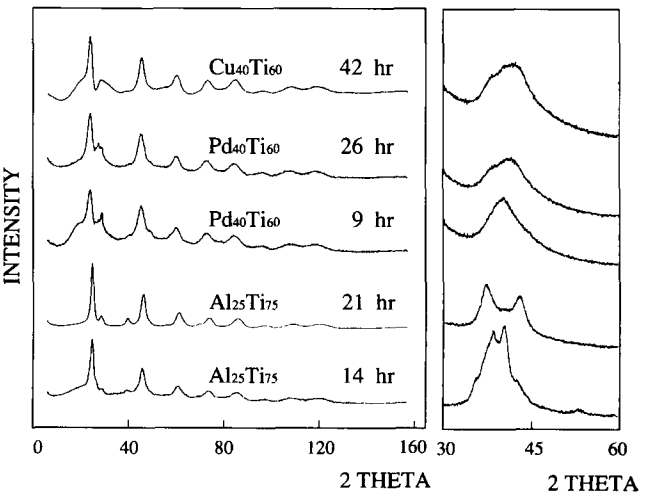

Fig. 5. Neutron diffraction patterns for a series of titanium-based mechanically alloyed specimens, showing the regular arrangement of Bragg peaks common to each. The X-ray diffraction patterns, through the first amorphous halo, are given on the right-hand side of the figure for the same sample materials.

the second feature at $2\theta = 26°$ corresponds to the first maximum in $S(Q)$ at $Q = 3$ Å^{-1}. The feature at $Q = 1.9$ Å^{-1} can also be detected in the patterns for $Pd_{40}Ti_{60}$ (9 h) and $Al_{25}Ti_{75}$ (14 h). The X-ray diffraction patterns for these five samples are quite different. That for $Pd_{40}Ti_{60}$ (9 h) shows a broad halo which would be universally accepted as evidence of an amorphous sample, whereas those for $Cu_{40}Ti_{60}$ (42 h) and $Pd_{40}Ti_{60}$ (26 h) show some slight, but not serious, asymmetry. The pattern for $Al_{25}Ti_{75}$ redrawn from Fig. 3 and that for $Al_{25}Ti_{75}$ (21 h) have reasonably well-resolved (broadened) Bragg peaks on the first halo. Thus observers having access to only one set of the diffraction patterns (X-ray or neutron) would come to quite different conclusions about the atomic scale structures of these specimens.

It is clear that the significant differences between the neutron and X-ray diffraction patterns for the same sample material must originate from differences in the scattering amplitudes of the alloy constituents for the two radiations. There are several parameters which can be used to quantify the differences between the two sets of curves in Fig. 5. Table 1 gives the squares of the scattering amplitudes of the constituent atoms of the present samples in ascending order, for both radiations. It shows, for example, that with X-rays (at $Q = 0$) the intensity scattered from a palladium atom is some 2000 times that from a hydrogen atom. However, with neutrons, the intensity scattered by hydrogen is compatible with the other elements and the factor between the strongest (N) and weakest (Ti) scatterer is only about 7.5. The nuclear scattering amplitude for nitrogen is, in fact, one of the largest of all the elements [11]. The average values of the squares of the scattering amplitudes $\langle b^2 \rangle$ can be used as a measure of the visibilities of the amorphous phases. Suitable combinations of the amplitudes b_+^2, b_-^2, where $b_+ = xb_A + (1-x)b_B$, can also be used to illustrate the relative magnitudes of the fundamental (b_+) and superlattice (b_-) peaks of the ordered phases (see ref. 4). These values are given in Table 2, which shows that with X-rays the light-atom amorphous alloy $Al_{25}Ti_{75}$ scatters less effectively than $Pd_{40}Ti_{60}$ or $Cu_{40}Ti_{60}$. More importantly, the hydride TiH_2, if present in small quantities, will be difficult to detect with X-rays in any of the amorphous phases, although the oxide and nitride TiO and TiN will be increasingly visible if present in $Al_{25}Ti_{75}$ and $Cu_{40}Ti_{60}$. This corresponds reasonably well to the form of the X-ray curves in Fig. 5 as described above. The factor between the strongest and weakest scatterer of the amorphous phases (3:1) is about the same for neutrons as for X-rays. However, the important difference is that the neutron scattering from titanium hydride, oxide and nitride is not only comparable, but may be greater, than that from the amorphous metallic phases. There are more sophisticated measures of the visibility of these different phases, which can incorporate atomic density values, absorption coefficients and other factors, but they would not change the basic conclusion from Tables 1 and 2 that the presence of TiO and TiN impurities in the amorphous mechanically alloyed phases will be much more visible with neutrons than with X-rays.

TABLE 1. Squares of the scattering amplitudes of the elemental alloy constituents for neutron and X-radiation

Element	X-Ray scattering $f^2(0) \times 10^{-24}$ (cm^2)	Element	Neutron scattering $b^2 \times 10^{-24}$ (cm^2)
H	0.08	Ti	0.1182
N	3.89	Al	0.1190
O	5.08	H	0.1400
Al	13.42	O	0.3370
Ti	38.43	Pd	0.349
Cu	66.78	Cu	0.5957
Pd	168.01	N	0.865

TABLE 2. Combinations of the scattering amplitudes illustrating the visibilities of the different phases for neutron and X-radiation

Amorphous phase	X-rays $\langle f(0)^2 \rangle \times 10^{-24}$ (cm^2)	Neutrons $\langle b^2 \rangle \times 10^{-24}$ (cm^2)
$Cu_{40}Ti_{60}$	49.77	0.3097
$Pd_{40}Ti_{60}$	90.26	0.2110
$Al_{25}Ti_{75}$	32.18	0.1184

Crystalline phase	$f_+^2(0) \times 10^{-24}$ (cm^2)	$f_-^2(0) \times 10^{-24}$ (cm^2)	$b_+^2 \times 10^{-24}$ (cm^2)	$b_-^2 \times 10^{-24}$ (cm^2)
TiH_2	5.08	3.53	0.1325	0.0182
TiO	17.86	3.89	0.0140	0.2136
TiN	16.69	4.46	0.0859	0.4056

The regular sequence of Bragg peaks seen in Fig. 5 is characteristic of a face-centred cubic structure with the Miller indices *hkl* all odd. The Bragg peak positions were evaluated using a simple program which marked the turning points in the intensity profile, and an average value of the lattice parameter was obtained by minimizing the sum $|2\theta_{obs} - 2\theta_{calc}|$ using the initial value of a_o obtained. The values of the lattice parameter derived for the five specimens are given in Table 3 and are close to the accepted values of both stoichiometric TiO (4.180 Å) and TiN (4.239 Å) [12]. The lack of an exact correspondence in the lattice parameters is not important. Both TiO and TiN can exist for a range of compositions and pseudo-binaries Ti(O, N) form easily due to the vacant sites in the substoichiometric TiO_x and TiN_x phases. Since both titanium oxide and titanium nitride have the O_h^5, $Fm3m$, NaCl-type structure, strong peaks with odd *hkl* are observed.

TABLE 3. Lattice parameters, temperature factors and integral peak breadths for the Ti(O, N) mixed phases found in the mechanically alloyed samples

Specimen and MA treatment	Lattice parameter ($Å^{-1}$) (± 0.004)	Temperature factor B ($Å^2$)	Integrated peak breadth (°)	$-2B/$ ln(breadth) ($Å^2$)
$Cu_{40}Ti_{60}$ 42 h	4.235	2.29	5.6	1.3
$Pd_{40}Ti_{60}$ 26 h	4.249	2.61	4.8	1.7
$Pd_{40}Ti_{60}$ 9 h	4.250	2.62	4.5	1.7
$Al_{25}Ti_{75}$ 21 h	4.210	3.42	6.1	1.9
$Al_{25}Ti_{75}$ 14 h	4.232	3.45	6.5	1.8
Stoichiometric TiN	4.239			
Stoichiometric TiO	4.180			

TABLE 4. Comparison of calculated and observed Bragg peak intensities for the Ti(O, N) phase in $Al_{25}Ti_{75}$ mechanically alloyed for 21 h as a function of $N=h^2+k^2+l^2$ and 2θ

N	2θ	I_{obs}	I_{cal} (TiO)	I_{cal} (TiN)	I_{cal} ($Ti(O_{0.4}N_{0.6})$)
3	22.5	41.6	43.5	37.5	39.4
4	26.1	3.6	1.5	4.4	3.4
8	37.2	3.7	1.3	3.7	2.9
11	43.9	21.7	24.5	21.6	22.4
12	46.0	abs	0.5	1.4	1.1
16	53.6	0.7	0.2	0.7	0.5
19	58.9	10.0	9.8	8.8	9.2
20	60.6	abs	0.6	1.8	1.3
24	67.1	0.8	0.4	1.2	0.9
27	71.7	6.4	6.5	5.9	6.1
32	79.3	abs	0.0	0.3	0.3
35	83.7	6.0	5.2	4.9	5.1
36	85.2	abs	0.2	0.6	0.5
40	91.0	abs	0.0	0.2	0.2
43	95.4	1.7	1.5	1.5	1.5
44	96.8	abs	0.0	0.3	0.2
48	102.0	abs	0.0	0.1	0.1
51	107.3	1.9	1.9	1.9	1.9
52	108.8	abs	0.0	0.2	0.2
56	115.1	abs	0.0	0.3	0.2
59	120.0	1.9	1.9	1.9	1.9
64	128.9	abs	0.0	0.0	0.0
67	134.8	abs	0.5	0.5	0.5
68	136.9	abs	0.0	0.2	0.1
72	146.2	abs	0.0	0.1	0.1

$I_{hkl}^{even} \propto (b_{Ti}+b_O)^2$ or $(b_{Ti}+b_N)^2$

$I_{hkl}^{odd} \propto (b_{Ti}-b_O)^2$ or $(b_{Ti}-b_N)^2$

Because b_{Ti} is negative I_{hkl}^{even} is small and I_{hkl}^{odd} is magnified as indicated in the lower part of Table 2. In order to confirm the identification made through Table 3 we have calculated the Bragg peak intensities for TiO, TiN and a mixed $Ti(O_{0.4}N_{0.6})$ phase. Table 4 gives typical results, in this case for the $Al_{25}Ti_{75}$ 21 h sample, which show that the level of agreement between calculation and observation is mostly satisfactory. The temperature factors for these calculations were of the usual form $\exp(-2B \sin^2 \theta/\lambda^2)$ so that plotting $\ln(I_{obs}/I_{calc})$ against $(\sin \theta/\lambda)^2$ gave the value of B for each sample and the scaling factor between I_{obs} and I_{calc}. The values of B might be expected to be the same for the five samples, given that roughly similar impurities have produced the Bragg peaks. However, Table 3 shows some variation in the B values. We believe that this is mainly due to the difficulty in defining the area (intensity) of the Bragg peaks when they are broad at high scattering angles. The fact that the integral width of the Bragg peaks (*e.g.* the value for $N=59$ given in Table 4) scales reasonably well with the temperature factor supports this hypothesis. The Bragg peak broadening is likely to arise from the local variation in oxygen and nitrogen concentration, strains from the MA process and crystallite size effects, but insufficient data exist to distinguish between these.

5. Thermodynamic considerations

The role of gaseous contaminants in the amorphization of titanium-based alloys by MA can be examined with reference to the Cu–Ti–H system for which a collection of thermodynamic data has been made [13]. A thermodynamic analysis of the ternary was made, employing the enthalpy data obtained in the present work, together with the free energy of formation of Cu–Ti intermetallics and crystalline hydrides (TiH_2, TiCuH, Ti_2CuH_3) reported in the literature. These compounds all lie on a ternary tie-line joining the $Cu_{66}Ti_{34}$ to TiH_2 compositions, along which the free energy of each phase can be evaluated. The heats of formation of the appropriate amorphous alloys were calculated as the difference between the heat of formation of their crystalline counterparts and their heat of crystallization. The entropies of formation were estimated in the same way by considering that the entropy change on crystallization of metallic alloys is not far from one-third of the entropy of fusion.

The resulting phase stability diagram at 300 K is shown in Fig. 6 where the free energies of mixtures of the compounds are represented by straight lines and that of the amorphous phase as a smoothed curve. Both the amorphous and the crystalline hydrogenated phases appear to be metastable with respect to a mixture of CuTi intermetallics and TiH_2. The free energy trend for the amorphous phase is consistent with the observation of a phase separation into two distinct amorphous structures which was made on glassy ribbons loaded with hydrogen either electrolytically or from the gas phase [14, 15]. Since our starting mixture for the

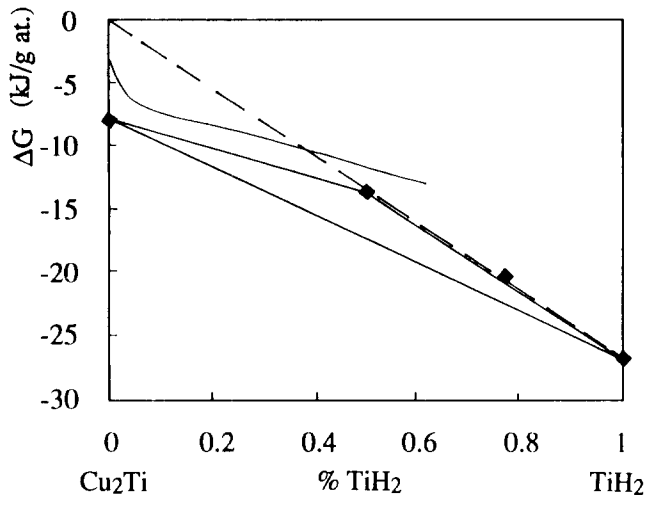

Fig. 6. Free energy diagram at 300 K for a section of the Cu–Ti–H ternary system along the Cu_2Ti–TiH_2 tie-line. The filled squares represent crystalline compounds, the curve represents the amorphous phase and the broken line gives the free energy of the unmixed components, *i.e.* Cu, Ti and TiH_2. Reference phases are Cu, Ti and gaseous H_2.

MA experiments was made of Cu and Ti containing 7.5 mol.% TiH_2, its free energy is given by the broken line in Fig. 6. It is evident that a driving force for the amorphization reaction exists at low hydrogen concentration, so that TiH_2 can be dissolved in the homogeneous amorphous phase. It is also clear that some TiH_2 remains unalloyed if the hydrogen content is significantly increased.

If we consider the effect of oxygen and nitrogen contamination, inspection of tabulated data [16] shows that the free energies of formation of TiO and TiN are 247 kJ (g atom)$^{-1}$ and -155 kJ (g atom)$^{-1}$ respectively. (Note that these values are significantly higher than the free energy of formation of TiH_2 which is -26.5 kJ (g atom)$^{-1}$. So, any fortuitous leak in either the glove box or the vial where the powders are milled will cause the preferential formation of these TiO and TiN compounds with respect to Cu–Ti alloys. A second source of contamination may be gases adsorbed on the powders before introduction into the vial. This has also been seen in further experiments performed on Cu–Ti alloys. When using powders kept under an inert atmosphere, amorphization was always achieved, but when using copper powder which had been exposed to the air for a prolonged time, a mixture of intermetallic compounds was obtained. If the same copper powder was then degassed at 550 °C and used for a third milling experiment, an amorphous phase was again produced [17].

Acknowledgments

This work was performed for Progetto Finalizzato CNR "Materiali Speciali per Tecnologie Avanzate" under contracts 89.00623.68 (Università di Sassari) and 89.00605.68 (Università di Torino). The collaboration between G.C. and N.C. was supported by a CNR/Royal Society Travel Grant. The neutron measurements were performed with the support of the Science and Engineering Research Council (SERC) and the help of Dr. P. Convert at ILL, Grenoble. J.H. acknowledges the support of an SERC studentship.

References

1 A. W. Weeber and H. Bakker, *Physica B, 153* (1988) 93–135.
2 M. Sakata, N. Cowlam and H. A. Davies, in T. Masumoto and K. Suzuki (eds.), *Proc. 4th Int. Conf. on Rapidly Quenched Metals,* Vol. 1, Japan Institute of Metals, Sendai, 1982, pp. 327–329.
3 P. K. Ivison, I. Soletta, N. Cowlam, G. Cocco, S. Enzo and L. Battezzati, *J. Phys. Condensed Matter, 4* (1992) 1635–1645.
4 P. K. Ivison, I. Soletta, N. Cowlam, G. Cocco, S. Enzo and L. Battezzati, *J. Phys. Condensed Matter, 4* (1992) 5239–5248.
5 G. Cocco, *Mater. Sci. Forum, 88–90* (1992) 703–710.
6 X. L. Yeh, K. Samwer and W. L. Johnson, *Appl. Phys. Lett., 42* (1983) 242–244.
7 K. Aoki, X.-G. Li, T. Aihara and T. Masumoto, *Mater. Sci. Eng. A, 133* (1991) 316–320.
8 G. Placzek, *Phys. Rev., 86* (1952) 377–388.
9 G. Cocco, L. Schiffini, I. Soletta, M. Baricco and N. Cowlam, *J. Phys. (Paris), Colloq., 4* (1990) 175–180.
10 M. Baricco, L. Battezzati, I. Soletta, L. Schiffini and N. Cowlam, *Mater. Sci. Eng. A, 134* (1991) 1398–1401.
11 G. E. Bacon, *Neutron Diffraction,* Oxford University Press, Oxford, 3rd edn., 1975.
12 P. Villars and L. D. Calvert, *Pearson's Handbook of Crystallographic Data for Intermetallic Phases,* Vol. 3, American Society for Metals, Metals Park, OH, 1985.
13 L. Battezzati, M. Baricco, G. Cocco, I. Soletta and S. Enzo, in A. R. Yavari (ed.), *Ordering and Disordering in Alloys,* Elsevier Applied Science, London, 1992, pp. 446–453.
14 B. Rodmacq, M. Maret, J. Laugier, L. Billarde and A. Charnberod, *Phys. Rev. B, 38* (1988) 1105–1115.
15 D. Manzel, A. Niklas and U. Koester, *Mater. Sci. Eng., A 133* (1991) 312–315.
16 R. C. Weast (ed.), *Handbook of Chemistry and Physics,* CRC Press, Boca Raton, FL, 1988.
17 I. Soletta, *Ph.D. Thesis,* Univeristy of Sassari, 1992.